An Efficiency Optimization Method Based on Double Side Impedance Angle Design for Wireless Power Transfer System

Zhan Sun, *Student Member, IEEE*, Jinwu Sun, Yijie Wang, *Senior Member, IEEE*, and Dianguo Xu, *Fellow, IEEE*

***Abstract*—Wireless power transfer (WPT) system has already been applied to battery charging occasions, and the charging process can be roughly divided into two stages: constant current mode (CCM) and constant voltage mode (CVM). In CVM, researchers always focus on the effect of the primary phase angle (PPA) on the system efficiency but rarely pay attention to secondary phase angle (SPA). A large SPA will also lead to a decrease of system efficiency, which should be worth more attention and consideration when designing the system parameter. The double-sided *LCC* compensation topology can not only achieve constant current or constant voltage output at different frequencies but also has the advantage of high parameter design freedom, so it is very suitable for battery charging scenarios. Considering the influence of the PPA and SPA on the system efficiency, a novel parameter design method based on double-sided *LCC* compensation topology is proposed in this article. By changing the system operating frequency, the switching between CCM and quasi-constant voltage mode (QCVM) is realized. In order to verify the feasibility and practical effect of the parameter design method, an experimental prototype based on a planar square coil was established and three groups of comparative experiments were conducted. The experimental results show that the optimized WPT system efficiency is significantly improved under the same power level. The maximum output power of the system is 620 W. When the optimized system works in CCM and QCVM, the maximum efficiency is about 95%.**

***Index Terms*—Battery charging, constant current/quasi-constant voltage mode (CCM/QCVM), double-sided *LCC* compensation, primary/secondary phase angle (PPA/SPA), wireless power transfer (WPT).**

NOMENCLATURE

U_{in}	System input voltage.
U_{o}	System output voltage.
I_{o}	System output current.
f_{CC}	Frequency in constant current mode.
f_{QCV}	Frequency in quasi-constant voltage mode.
f_{CV}	Frequency in constant voltage mode.
L_1	Self-inductance of primary coil.
L_2	Self-inductance of secondary coil.
M	Mutual inductance.
k	Coupling coefficient.
L_{f1}	Primary compensation inductance.
L_{f2}	Secondary compensation inductance.
C_{f1}	Primary parallel compensation capacitor.
C_{f2}	Secondary parallel compensation capacitor.
C_1	Primary series compensation capacitor.
C_2	Secondary series compensation capacitor.
φ_{p}	Primary impedance angle.
φ_{pa}	Primary impedance angle expression numerator corresponding phase angle.
φ_{pb}	Primary impedance angle expression denominator corresponding phase angle.
φ_{s}	Secondary impedance angle.
φ_{sa}	Secondary impedance angle expression numerator corresponding phase angle.
φ_{sb}	Secondary impedance angle expression denominator corresponding phase angle.
U_{f}	Voltage fluctuation rate.
$SP_{\varphi\text{s-Cf2}}$	Change rate of φ_{s} relative to C_{f2} when f_{QCV} is fixed.
$SP_{\varphi\text{s-C2}}$	Change rate of φ_{s} relative to C_2 when f_{QCV} is fixed.
$SP_{\varphi\text{p-Cf1}}$	Change rate of φ_{p} relative to C_{f1} when f_{QCV} is fixed.
$SP_{\varphi\text{p-C1}}$	Change rate of φ_{p} relative to C_1 when f_{QCV} is fixed.
$SP_{\varphi\text{s-fQCV}}$	Change rate of φ_{s} relative to f_{QCV} when C_2 or C_{f2} is fixed.
$SP_{\varphi\text{p-fQCV}}$	Change rate of φ_{p} relative to f_{QCV} when C_1 or C_{f1} is fixed.
η	System efficiency.

Manuscript received 17 November 2022; accepted 21 December 2022. Date of publication 27 December 2022; date of current version 14 February 2023. This work was supported in part by the National Natural Science Foundation of China under Grant 51922033, in part by the Power Electronics Science and Education Development Program of Delta Group under Grant DREK2020003, and in part by the Natural Science Foundation of Heilongjiang Province under Grant YQ2020E017. Recommended for publication by Associate Editor M. Ponce-Silva. *(Corresponding author: Yijie Wang.)*

The authors are with the School of Electrical Engineering and Automation, Harbin Institute of Technology, Harbin 150001, China (e-mail: 21b906030@stu.hit.edu.cn; 21s006089@stu.hit.edu.cn; wangyijie@hit.edu.cn; xudiang@hit.edu.cn).

Color versions of one or more figures in this article are available at https://doi.org/10.1109/TPEL.2022.3232415.

Digital Object Identifier 10.1109/TPEL.2022.3232415

I. INTRODUCTION

AS A new type of power transmission, wireless power transfer (WPT) has developed rapidly in recent years. Because of its flexibility, convenience, electrical isolation, good environmental adaptability, and convenient maintenance, it is

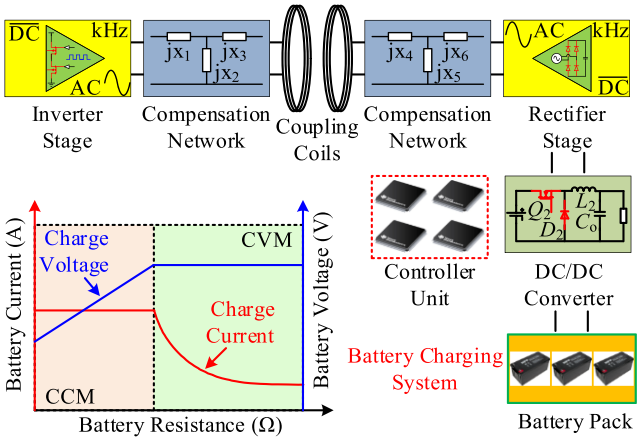

Fig. 1. Battery charging system with WPT technology.

widely used in the fields of implantable medical treatment, solar cell array driving device, consumer electronics, and autonomous underwater vehicle [1], [2], [3], [4], [5], [6], [7]. Fig. 1 shows the structure of a typical battery charging system based on WPT technology, which mainly includes eight parts: inverter, primary compensation, coupling coils, secondary compensation, rectifier, dc/dc converter, battery pack, and controller.

Different from the traditional wired charging system, the coupling coil of the WPT system usually has a large leakage inductance, which often brings undesired reactive power components. Therefore, it is necessary to add a compensation network to improve the system power transfer efficiency. According to the output characteristics, the compensation network can be divided into two types: constant current output type and constant voltage output type. Among the four basic compensation networks (S/S, S/P, P/S, and P/P), P/S can provide constant voltage output characteristic, P/P can provide constant current output characteristic. S/S and S/P can both provide the two output characteristics [8], [9], [10], [11]. Based on the detailed analysis of four kinds of low-order compensation networks, a hybrid compensation method was proposed [10]. Furthermore, a series of higher order compensation networks with constant voltage or current output have been successively proposed [12].

When charging the battery, the WPT system usually needs to operate in two modes successively: constant current mode (CCM) and constant voltage mode (CVM). By switching the *CLC–LCL* network to the *CLC* network, the conversion between the system's constant current output capability and constant voltage output capability was achieved [13]. Certainly, mode switching was achieved by changing the secondary circuit topology, which requires three additional bidirectional switches, and it will inevitably lead to an increase in system cost. Meanwhile, the system needs to be shut down before switching the working mode, which results in limited application scenarios [14].

In the WPT system, power transfer efficiency is an extremely important indicator. Therefore, researchers have proposed many optimization methods for efficiency improvement. On the one hand, the purpose of efficiency optimization is achieved by adding additional components. For example, an input-series inductor was proposed to improve the phase angle of the load and achieved a 1.05% increase in system efficiency [15]. By connecting a capacitor in parallel with the input side of the rectifier to greatly compress the input impedance angle variation, the system efficiency was finally improved by 0.6% [16]. On the other hand, it is to improve the system efficiency by optimizing the existing design method. An improved winding and a novel compensation method were proposed [17]. At light load, the system efficiency was improved by 2.48% compared with the traditional method. With S/S compensation, a parameter design method based on loosely coupled transformers and resonant capacitors was proposed, and the maximum efficiency of the system can even reach 98% [18].

Previous studies have mainly focused on the realization of the zero-phase angle (ZPA) of the primary side [19], [20], [21], [22], [23], [24] (i.e., the input impedance angle is zero), but little attention was paid to the secondary side impedance angle. A tuning scheme for the WPT system based on the impedance decoupling algorithm was proposed in [25]. By adjusting the system frequency and the phase shift angle of the semiactive rectifier, the impedance angle on both sides can be zero. A self-adaptive capacitor matrix with a window prediction searching algorithm aiming at variable air gaps was proposed in [26]. By changing the resonant capacitance value, the impedance angle of the primary and secondary sides can be adjusted adaptively when the mutual inductance changes. In [27], an automatic tuning method using an L-type impedance matching network consisting of several capacitors and inductors was proposed. Use the impedance characteristics of the L-type matching network at different frequencies to adjust the primary and secondary side impedance angles. A capacitor switched by the amplifier based on the negative impedance converter was proposed in [28]. A control strategy with two-degree freedoms for the SAR was proposed in [29], where the pulse width and the phase shift angle were employed to adjust the load.

In this article, a novel method based on the designing of double side phase angle is proposed to optimize the efficiency of the WPT system compensated by double-sided *LCC* topology. The primary side impedance angle and the secondary side impedance angle are considered comprehensively. Through this method, the optimal efficiency design parameters under the current power level can be obtained according to the given input and output indicators. In practical applications, WPT systems usually need to be connected in series with a dc–dc circuit to keep the output constant. Therefore, in this design, the output voltage of double-sided *LCC* compensation is allowed to vary within a certain range, and it is named that the WPT system works in quasi-constant voltage mode (QCVM) at this time.

The rest of this article is organized as follows. The impedance characteristics of the WPT system based on double-sided *LCC* compensation are analyzed and the impedance angle formula is derived in Section II. In Sections III and IV, the specific parameter design flowchart is given, and the rationality of the proposed design method is also analyzed in detail. Through the constraints of voltage adjustment capability, impedance angle range boundary, and system parameter sensitivity, the optimal parameter group under the experimental conditions of this article

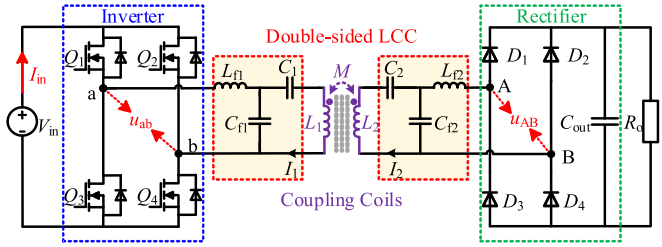

Fig. 2. Typical WPT system based on double-sided *LCC* compensation.

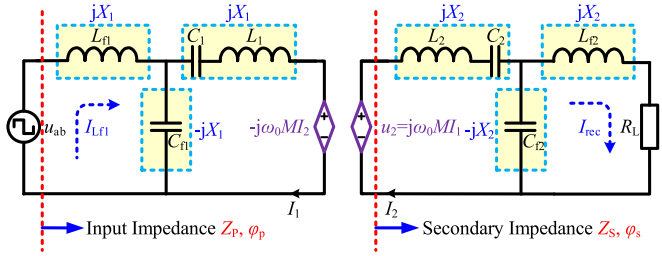

Fig. 3. Equivalent circuit diagram of the double-sided *LCC* compensation system.

is finally determined. In Section V, an experimental prototype is built and three sets of comparative experiments are carried out. Through detailed result analysis, the effectiveness of the proposed design method is verified. Finally, Section VI concludes this article.

II. Analysis of Double-Sided *LCC* Compensation Topology and Double Side Impedance Angle

Double-sided *LCC* compensation has many advantages, such as the constant current output characteristic is independent of the load and zero voltage switching can be easily achieved. Generally, a typical WPT system based on double-sided *LCC* compensation topology consists of a full-bridge inverter, double-sided *LCC* compensation, coupling coils, full-bridge rectifier, and load as shown in Fig. 2, where L_{f1} and L_{f2} are compensation inductances, C_{f1} and C_{f2} are parallel compensation capacitors, C_1 and C_2 are series compensation capacitors, L_1 and L_2 are the primary and secondary self-inductances, M is the mutual inductance of the coupling coils, and R_o is the load.

The analysis of double-sided *LCC* compensation topologies has been extensively studied. The formulas of input current, output current, and compensation inductance current have been derived in [30]. The principle of the constant voltage output of double-sided *LCC* compensation and the operating state of the resonator were analyzed. Furthermore, the corresponding expression of output voltage was also deduced [31]. Using a controlled source equivalent model for analysis, the equivalent circuit of the WPT system with double-sided *LCC* compensation is shown in Fig. 3, where Z_p and Z_s represent input impedance and secondary impedance, respectively, and R_L is the equivalent input resistance of the rectifier. According to the tuning method

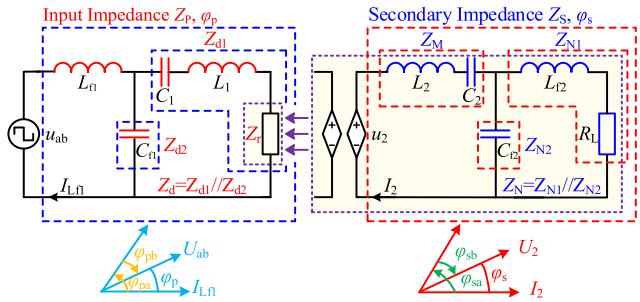

Fig. 4. Schematic diagram of double-sided LCC impedance and vector.

of the double-sided *LCC* compensation network in [34], compensation capacitors can be defined by

$$\begin{cases} C_{f1} = \frac{1}{\omega_0^2 L_{f1}}, C_1 = \frac{1}{\omega_0^2 (L_1 - L_{f1})} \\ C_{f2} = \frac{1}{\omega_0^2 L_{f2}}, C_2 = \frac{1}{\omega_0^2 (L_2 - L_{f2})}. \end{cases} \tag{1}$$

The load-independent constant current output characteristic can be described by

$$I_{rec} = \frac{M U_{ab}}{\omega_0 L_{f1} L_{f2}}. \tag{2}$$

This article mainly studies the relationship between Z_p, Z_s and system efficiency, and further proposes an efficiency optimal method based on double side impedance angle design. Therefore, the expression for the impedance angle needs to be obtained first, to facilitate the analysis of the impedance angle. As shown in Fig. 4, define Z_{N1} and Z_{N2} as follows:

$$Z_{N1} = j\omega_0 L_{f2} + R_L, Z_{N2} = \frac{1}{j\omega_0 C_{f2}}. \tag{3}$$

The expression of Z_N is

$$Z_N = Z_{N1} // Z_{N2} = \frac{j\omega_0 L_{f2} + R_L}{-\omega_0^2 L_{f2} C_{f2} + j\omega_0 C_{f2} R_L + 1}. \tag{4}$$

Define Z_M as follows:

$$Z_M = j\omega_0 L_2 + \frac{1}{j\omega_0 C_2} = \frac{-\omega_0^2 L_2 C_2 + 1}{j\omega_0 C_2}. \tag{5}$$

So far, the expression of Z_s can be obtained as follows:

$$Z_s = Z_N + Z_M. \tag{6}$$

Substitute (4) and (5) into (6) to obtain (7) shown at the bottom of the next page. Furthermore, secondary impedance angle φ_s can be obtained by the arctangent operation of Z_s. Take the numerator and denominator phase angle in (7) as two impedance angles φ_{sa} and φ_{sb}, respectively (see Fig. 4), then φ_s can be described by (8)

$$\varphi_s = \varphi_{sa} - \varphi_{sb} \tag{8}$$

where φ_{sa} and φ_{sb} are described in (9) shown at the bottom of the next page. To simplify the above-mentioned formulas, A_s,

B_s, C_s, and D_s are defined as follows:

$$\begin{cases} A_s = 1+\omega_0^4 L_2C_2L_{f2}C_{f2}-\omega_0^2 L_2C_2-\omega_0^2 L_{f2}C_{f2}-\omega_0^2 L_{f2}C_2 \\ B_s = -\omega_0^3 L_2C_2C_{f2}R_L+\omega_0 C_{f2}R_L+\omega_0 C_2R_L \\ C_s = -\omega_0^2 C_2C_{f2}R_L, D_s = -\omega_0^3 C_2C_{f2}L_{f2}+\omega_0 C_2. \end{cases} \tag{10}$$

Then, (7) can be simplified as

$$Z_s = \frac{A_s + B_s\mathrm{j}}{C_s + D_s\mathrm{j}}. \tag{11}$$

Also, φ_s can be obtained as

$$\varphi_s = \arctan\frac{B_s}{A_s} - \arctan\frac{D_s}{C_s}. \tag{12}$$

The equivalent reflection impedance on the secondary side Z_r can be represented by

$$Z_r = \frac{(\omega_0 M)^2}{Z_s} = A_r + \mathrm{j}A_i = \frac{(\omega_0 M)^2}{A_s^2+B_s^2}(A_sC_s + B_sD_s) + \mathrm{j}\frac{(\omega_0 M)^2}{A_s^2+B_s^2}(A_sD_s - B_sC_s). \tag{13}$$

Similarly, define Z_{d1} and Z_{d2} as follows:

$$Z_{d1} = \frac{1}{\mathrm{j}\omega_0 C_1} + \mathrm{j}\omega_0 L_1 + Z_r, Z_{d2} = \frac{1}{\mathrm{j}\omega_0 C_{f1}}. \tag{14}$$

Then, Z_p can be expressed as

$$Z_p = \mathrm{j}\omega_0 L_{f1} + Z_d = \mathrm{j}\omega_0 L_{f1} + Z_{d1}//Z_{d2}. \tag{15}$$

The expression of Z_d is given by (16) shown at the bottom of the next page. By substituting (16) into (15), the expression of Z_P containing primary parameters (L_1, L_{f1}, C_{f1}, C_1, and Z_r) can be obtained, as shown in (17). Then, the primary impedance angle φ_p can be obtained by the arctangent operation of Z_p. Take the numerator and denominator phase angle in (17) shown at the bottom of the next page, as two impedance angles φ_{pa} and φ_{pb}, respectively (see Fig. 4), φ_p can be further described by (18)

$$\varphi_p = \varphi_{pa} - \varphi_{pb} \tag{18}$$

where φ_{pa} and φ_{pb} are described in (19) shown at the bottom of the next page. To further simplify (17), define A_p, B_p, C_p, and D_p as follows:

$$\begin{cases} A_p = \omega_0^4 C_1L_1L_{f1}C_{f1} - \omega_0^2\left(C_1L_{f1}+L_{f1}C_{f1}+C_1L_1\right) \\ \qquad + \left(\omega_0^2 L_{f1}C_{f1}-1\right)\omega_0 C_1A_i + 1 \\ B_p = \omega_0 C_1\left(1-\omega_0^2 L_{f1}C_{f1}\right)A_r, C_p = -\omega_0^2 C_{f1}C_1A_r \\ D_p = -\omega_0^3 C_{f1}C_1L_1 - \omega_0^2 C_{f1}C_1A_i + \omega_0(C_1+C_{f1}) \end{cases} \tag{20}$$

where A_r and A_i are derived in (13). Hence, Z_p and φ_p can be simplified as follows:

$$Z_p = \frac{A_p + B_p\mathrm{j}}{C_p + D_p\mathrm{j}}, \varphi_p = \arctan\frac{B_p}{A_p} - \arctan\frac{D_p}{C_p}. \tag{21}$$

So far, the expressions of the secondary side impedance angle and the primary side impedance angle have been deduced in detail and simplified. The design method of compensation parameters (L_{f1}, C_{f1}, C_1, L_{f2}, C_{f2}, C_2) and coil parameters (L_1, L_2) to achieve maximum efficiency under CCM and QCVM will be presented in the following section, when the system input and output indicators (V_{in}, V_{out}, I_o) are specified.

III. Design Method of Optimal Efficiency

Based on the theoretical derivation in Section II, we propose a novel parameter design optimization method, the specific process of which is shown in Fig. 5. In practical application, the WPT system is only a part of the whole power supply system. When designing the WPT system, it is necessary to first determine the output voltage of the preceding circuit, which also is the input voltage of the WPT system, and then determine the output parameters of the WPT system as the input of the following circuit (such as dc–dc circuit). In this article, V_{in} is the dc input voltage of WPT system. I_o is the required charging current, which is also the output current of WPT system working at CCM based on double-sided *LCC* compensation. Generally, WPT system always needs a dc–dc circuit at the output end to prevent output change due to coupling coefficient variation and other reasons, so as to achieve constant output current or voltage. Therefore, the proposed method allows the system output voltage to fluctuate within a certain range as long as the dc–dc circuit can work efficiently. Hence, V_o is the required output voltage, which also is the minimum output voltage when the WPT system working in QCVM. After referring to the load variation range in [32], it is assumed that the load changes from 20 to 40 Ω in CCM and 40 to 200 Ω in QCVM in this design. To verify the proposed parameter design method, a prototype with an output power of about 600W is planned to be built, the input voltage is set to 200 V, the output current is set to 4 A, and the output voltage is set to 160 V. So far, the power level is determined according to the input and output parameters required by the system and the load variation range. The appropriate core and litz wire can be selected according to the power level.

Second, coil parameters, compensation inductance, and operating frequency range need to be determined. With reference to the coil self-inductance adopted in [31] and [35] and the target power designed in this article, it is decided to set the

$$Z_s = \frac{\omega_0^4 L_2C_2L_{f2}C_{f2} - \mathrm{j}\omega_0^3 L_2C_2C_{f2}R_L - \omega_0^2 L_2C_2 - \omega_0^2 L_{f2}C_{f2} - \omega_0^2 L_{f2}C_2 + \mathrm{j}\omega_0 C_{f2}R_L + \mathrm{j}\omega_0 C_2R_L + 1}{-\mathrm{j}\omega_0^3 C_2C_{f2}L_{f2} - \omega_0^2 C_2C_{f2}R_L + \mathrm{j}\omega_0 C_2} \tag{7}$$

$$\varphi_{sa} = \arctan\frac{\left(-\omega_0^2 L_2C_2C_{f2} + C_{f2} + C_2\right)\omega_0 R_L}{1+\omega_0^4 L_2C_2L_{f2}C_{f2} - \omega_0^2 L_2C_2 - \omega_0^2 L_{f2}C_{f2} - \omega_0^2 L_{f2}C_2}, \varphi_{sb} = \arctan\frac{-\omega_0^2 C_{f2}L_{f2}+1}{-\omega_0 C_{f2}R_L} \tag{9}$$

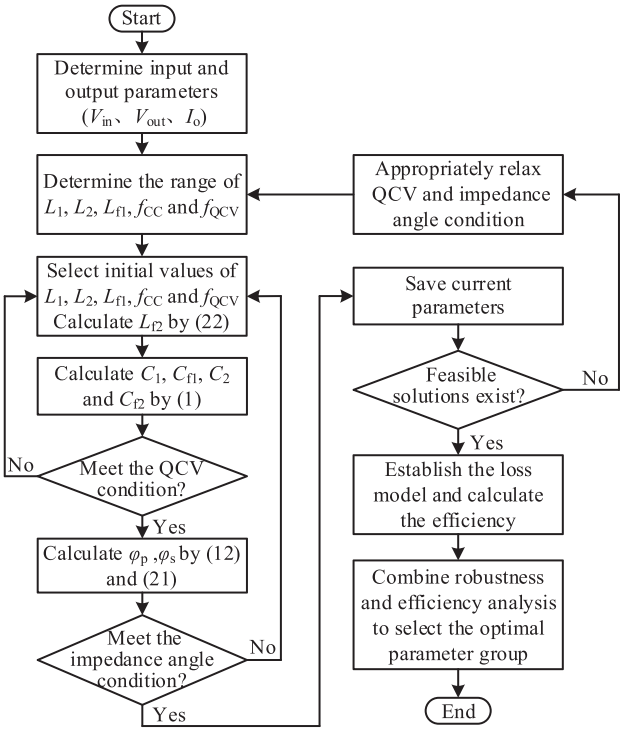

Fig. 5. System design block diagram.

self-inductance range of the primary and secondary coils (i.e., L_1 and L_2) to 100–150 μH and the range of compensation inductance to 40–70 μH. It should be noted that there are two compensation inductors (namely, L_{f1} and L_{f2}). Only one of them needs to be determined in this step, and the other can be calculated according to the subsequent steps. This article chose to determine the primary compensation inductance value (L_{f1}). In the existing research, the coupling coefficient of the primary and secondary coils is generally within the range of 0.1–0.4. The coupling coefficient is not the focus of this study, so it is taken as 0.25, which is easy to achieve. After determining the self-inductance and coupling coefficient of the coil, the value of mutual inductance M can be obtained accordingly. The current internationally recommended operating frequency of the WPT system is 85 kHz. Therefore, the selection of the operating frequency range of the system is based on 85 kHz. On the one hand, too low operating frequency will lead to excessive volume of compensation topology and rise of voltage and current stress of components. On the other hand, too high operating frequency will lead to greater parasitic resistance of the coil and increased switching loss. Therefore, the operating frequency range cannot be too wide. Furthermore, another consideration is that when the operating frequency range is narrow, the algorithm may not get a feasible solution. Based on the above considerations, the range of f_{CC} and f_{QCV} is determined as 50–170 kHz. Here, f_{CC} and f_{QCV} are the operating frequencies under CCM and QCVM, respectively.

Third, determine the initial value of the parameters according to the value range of the previous step. For example, the initial values of $L_1, L_2, L_{f1}, f_{CC}, f_{QCV}$ are $L_{10}, L_{20}, L_{f10}, f_{CC0}, f_{QCV0}$, which are the minimum value in the selected range. Using the fundamental analysis method, L_{f20} can be determined as follows:

$$L_{f20} = \frac{V_{in}}{I_o}\frac{k\sqrt{L_{10}L_{20}}}{\omega_{CC0}L_{f10}}\frac{8}{\pi^2}, \omega_{CC0} = 2\pi f_{CC0}. \tag{22}$$

Fourth, calculate C_1, C_{f1}, C_2, and C_{f2} by (1) using f_{CC0}, the results are also recorded as C_{10}, C_{f10}, C_{20}, and C_{f20}. So far, the system meeting the input and constant current output conditions has been built. Then, the calculation of the output voltage is carried out. Specifically, the output voltage value can be obtained according to (23). Substituting the initial values of each parameter taken in the third and fourth steps into the formulas in Section II, Z_{s0}, Z_{p0}, Z_{d10}, Z_{d20}, Z_{N10}, and Z_{N20} can be obtained accordingly

$$\begin{cases} U_o = \frac{R_L V_{in}\omega_{QCV0}k\sqrt{L_{10}L_{20}}}{Z_{p0}Z_{s0}}\frac{Z_{d20}}{Z_{d10}+Z_{d20}}\frac{Z_{N20}}{Z_{N10}+Z_{N20}} \\ \omega_{QCV0} = 2\pi f_{QCV0}. \end{cases} \tag{23}$$

When R_o changes within the previously specified range (40–200 Ω), the output voltage U_o will also change accordingly. Assume that U_{max} is the maximum value of the output voltage when the load changes as well as U_{min} is the minimum value, the voltage fluctuation rate U_f can be defined as follows:

$$U_f = \frac{U_{max} - U_{min}}{\frac{U_{max}+U_{min}}{2}}. \tag{24}$$

If U_f <0.5, the current parameters meet the QCV condition, because the dc–dc circuit can efficiently stabilize the output voltage. If the current parameters meet the QCV condition, then proceed to step 5. If not, return to step 3 to regain relevant parameter values.

Fifth, calculate φ_p,φ_s by (12) and (21). It is worth noting here that under QCVM, since the system works in a nonresonant state, the double-sided *LCC* compensation structure has been

$$Z_d = Z_{d1}//Z_{d2} = \frac{1 - \omega_0^2 L_1 C_1 + j\omega_0 C_1 Z_r}{-j\omega_0^3 L_1 C_1 C_{f1} - \omega_0^2 C_1 C_{f1} Z_r + j\omega_0 C_1 + j\omega_0 C_{f1}} \tag{16}$$

$$Z_p = \frac{\omega_0^4 L_1 C_1 L_{f1} C_{f1} - j\omega_0^3 C_1 L_{f1} C_{f1} Z_r - \omega_0^2 C_1 L_{f1} - \omega_0^2 C_{f1} L_{f1} - \omega_0^2 C_1 L_1 + j\omega_0 C_1 Z_r + 1}{-j\omega_0^3 L_1 C_1 C_{f1} - \omega_0^2 C_1 C_{f1} Z_r + j\omega_0 C_1 + j\omega_0 C_{f1}} \tag{17}$$

$$\varphi_{pa} = \arctan\frac{\left(-\omega_0^2 C_1 L_{f1} C_{f1} + C_1\right)\omega_0 Z_r}{\omega_0^4 L_1 C_1 L_{f1} C_{f1} - \omega_0^2 C_1 L_{f1} - \omega_0^2 C_{f1} L_{f1} - \omega_0^2 C_1 L_1 + 1}, \varphi_{pb} = \arctan\frac{-\omega_0^2 L_1 C_1 C_{f1} + C_1 + C_{f1}}{-\omega_0 C_1 C_{f1} Z_r} \tag{19}$$

transformed into a bilateral T-type impedance compression network for impedance angle compression. Typically, the bilateral impedance angle is expected to be smaller, resulting in better efficiency. But in fact, its impedance compression ability has a certain limit. Certainly, it can be greatly enhanced by dynamic impedance compression networks, such as variable inductors, variable capacitors, and capacitor matrices. However, this will inevitably bring additional device and system complexity. In addition, this is not the focus of this design. In the proposed design method, it is more desirable to optimize the efficiency of the WPT system through fixed parameters to reduce the complexity of the control. Therefore, in the case of limited impedance compression capability, the optimization of system efficiency near the maximum power point becomes a more prioritized choice [36]. Specifically, under QCVM (40–200 Ω), the power decreases correspondingly as the resistance increases, so the impedance angle variation near the mode switching point (40 Ω) is of more concern to us. In other words, under QCVM, when the efficiency of the maximum power point is improved, the efficiency of other power points will also be improved accordingly.

Generally, in order to achieve high efficiency of the system, zero-voltage turn-ON of the inverter is essential, and this usually requires a current that lags behind the voltage to discharge the energy of the parasitic capacitance of the switch. In other words, for the primary impedance angle φ_{p}, it needs to be greater than 0 to provide a weak inductive load. Certainly, the angle of lag is not the bigger the better, a larger impedance angle is bound to cause a large amount of reactive power loss, which will increase the voltage and current stress of each component, increase the loss of parasitic effects (such as the parasitic resistance of the coil), and ultimately reduce the system efficiency. Therefore, it is necessary to set the upper limit of the impedance angle.

In this article, the impedance angle of the primary and secondary sides is comprehensively considered, and the goal is to optimize the overall efficiency of the WPT system. According to the research and analysis in [31], if the WPT system based on double-sided *LCC* compensation works in CVM and achieves ZPA at the same time, the secondary impedance angle will be large. In this case, even if ZPA is realized, the decrease of system efficiency caused by the large impedance angle on the secondary side has not been reasonably solved, and there is still a large room for improvement. Therefore, a very severe ZPA is not required for the design method presented in this article. Instead, both sides of the impedance angle are within a reasonable range is what we care about. Based on the above analysis, the final impedance angle selection range is determined as follows:

$$\begin{cases} 0 < \varphi_{\mathrm{p}} < 0.6\,\mathrm{rad} \\ |\varphi_{\mathrm{s}}| < 0.7\,\mathrm{rad} \end{cases}. \tag{25}$$

If the impedance angle condition is met, the current parameters will be retained as a candidate group. If not, return to step 3. After conducting a lot of simulations, it can be found that there will always be an optimal solution within the range specified in (25). Furthermore, it should be noted that (25) is applicable to the experiment designed in this article, and can be appropriately changed for different power levels and input/output conditions.

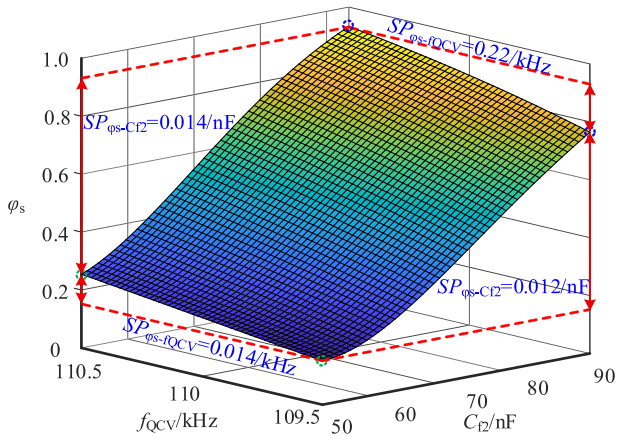

Fig. 6. Curved surface of secondary impedance angle varying with C_{f2} and f_{QCV}.

Sixth, after traversing all parameters, check whether there are feasible solutions. If there is no feasible solution, then relax QCV and impedance angle condition and return to the second step. Otherwise, establish the loss model according to the current parameters by using the method in [33]. Calculate the resonator efficiency of each candidate group.

Finally, the parameter groups with higher efficiency are selected among all candidate groups. Meanwhile, combined with the analysis of system efficiency and robustness (see the following section), the optimal parameter group is finally determined.

IV. Simulation and Sensitivity Analysis

In the WPT system, the optimal pursuit of efficiency is on the one hand, but on the other hand, it is worth considering how to maintain the robustness of the system with high efficiency as the output changes. Due to the error between the actual value and nominal value of capacitance and other factors, it is difficult to make the actual parameters consistent with the ideal designed parameters. Therefore, the sensitivity of the impedance angle to compensation parameters must be analyzed before determining the optimal efficiency point. Define sensitive parameters as follows:

$$\begin{cases} SP_{\varphi\mathrm{s-Cf2}} = \frac{\varphi_{\mathrm{s-max}}-\varphi_{\mathrm{s-min}}}{C_{\mathrm{f2-max}}-C_{\mathrm{f2-min}}}, SP_{\varphi\mathrm{s-C2}} = \frac{\varphi_{\mathrm{s-max}}-\varphi_{\mathrm{s-min}}}{C_{2\mathrm{-max}}-C_{2\mathrm{-min}}} \\ SP_{\varphi\mathrm{p-Cf1}} = \frac{\varphi_{\mathrm{p-max}}-\varphi_{\mathrm{p-min}}}{C_{\mathrm{f1-max}}-C_{\mathrm{f1-min}}}, SP_{\varphi\mathrm{p-C1}} = \frac{\varphi_{\mathrm{p-max}}-\varphi_{\mathrm{p-min}}}{C_{1\mathrm{-max}}-C_{1\mathrm{-min}}} \\ SP_{\varphi\mathrm{s-fQCV}} = \frac{\varphi_{\mathrm{s-max}}-\varphi_{\mathrm{s-min}}}{f_{\mathrm{QCV-max}}-f_{\mathrm{QCV-min}}} \\ SP_{\varphi\mathrm{p-fQCV}} = \frac{\varphi_{\mathrm{p-max}}-\varphi_{\mathrm{p-min}}}{f_{\mathrm{QCV-max}}-f_{\mathrm{QCV-min}}} \end{cases} \tag{26}$$

where taking $SP_{\varphi\text{s-Cf2}}$ as an example, it means the change rate of φ_{s} relative to C_{f2} when f_{QCV} is fixed. The interpretation of the meaning of other sensitivity parameters is also similar. At first, the influence of C_{f2} and f_{QCV} on φ_{s} is analyzed. It can be seen from Fig. 6 that φ_{s} changes 0.014 as C_{f2} changes 1 nF when $f_{\mathrm{QCV}} = 110.5$ kHz; when operating at 109.5 kHz, the value of $SP_{\varphi\text{s-Cf2}}$ is 0.012/nF; when $C_{\mathrm{f2}} = 90$ nF, φ_{s} changes 0.22 as f_{QCV} changes 1 kHz. When changing to 50 nF, $SP_{\varphi\text{s-fQCV}}$ changes to 0.014/kHz. Then, the influence of C_2 and f_{QCV} on φ_{s} is analyzed, which can be seen from Fig. 7. When C_2 changes,

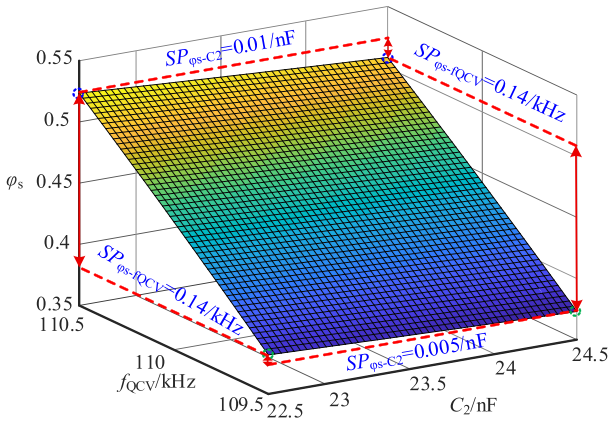

Fig. 7. Curved surface of secondary impedance angle varying with C_2 and f_{QCV}.

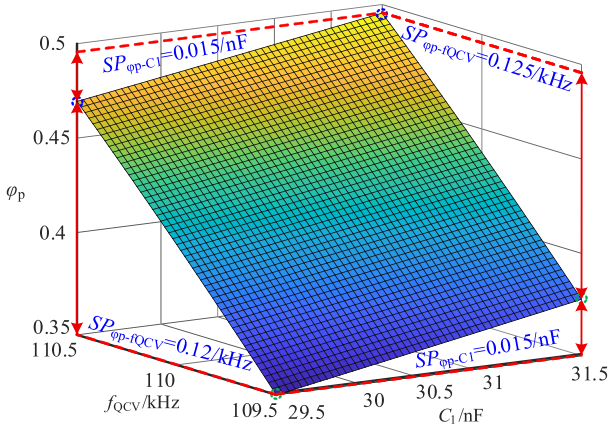

Fig. 8. Curved surface of primary impedance angle varying with C_1 and f_{QCV}.

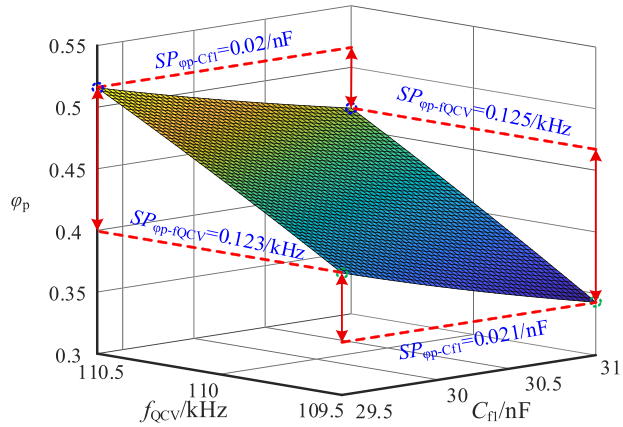

Fig. 9. Curved surface of primary impedance angle varying with C_{f1} and f_{QCV}.

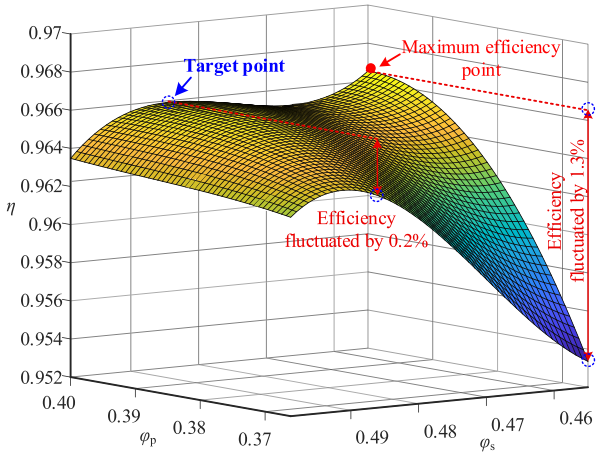

Fig. 10. System efficiency versus double side impedance angles.

$SP_{\varphi s\text{-}fQCV}$ is almost stable and always maintains 0.14/kHz; when f_{QCV} is 110.5 kHz, φ_s changes 0.01 as C_2 changes 1nF; and φ_s changes 0.005 as C_2 changes 1nF when $f_{QCV} = 109.5$ kHz. The sensitivity of the primary impedance angle to the primary compensation can be analyzed by the same way (as shown in Figs. 8 and 9). Comparing Figs. 6 and 9, it can be found that the primary impedance angle is more sensitive to the change of compensation parameters. The same conclusion can also be obtained by comparing Figs. 7 and 8. Actually, in practice applications, f_{QCV} is usually generated and controlled by a digital signal processor (DSP) with almost no error. More attention should be paid to the error caused by the compensation capacitance to the system design.

In order to facilitate the robust analysis of the system efficiency, the parameter sensitivity is unified as the relationship between the primary and secondary impedance angles and the system efficiency. Define η as the system efficiency. According to the process shown in Fig. 5, η-φ_p-φ_s surface graph under QCVM can be obtained to select the optimal parameters. It can be seen from Fig. 10 that the highest efficiency occurs near the point ($\varphi_p = 0.40$ rad, $\varphi_s = 0.455$ rad). Although the efficiency is the maximum at this point, it is very sensitive to the change of φ_p. When φ_s is fixed (0.455 rad), if φ_p changes by 0.033 rad, η will change by 1.3%. However, when $\varphi_s = 0.485$ rad, the system efficiency hardly decreases with the change of φ_p. If φ_p changes by 0.033 rad, η will only change by 0.2%. Furthermore, the maximum efficiency is only lower than the former less than 0.1%, but the robustness of the system efficiency has been greatly improved. According to the above analysis, the target point with high efficiency and strong robustness at the same time (i.e., $\varphi_p = 0.40$ rad and $\varphi_s = 0.485$ rad for this design) is more suitable as the mode switching point (the maximum power point under QCVM, 40 Ω for this design), and the candidate group that can reach this target point or close to this target point will be the final optimal parameter group.

V. Experimental Verification

In order to verify the effectiveness of the method proposed in this article, three groups of experiments were conducted, named as Group 1, Group 2, and Group 3, respectively. The three sets of parameters all work in the resonant state in the CCM mode, but they are different in the constant voltage stage. Among them, Group 1 is the optimal efficiency solution under

TABLE I
THREE GROUPS OF EXPERIMENTAL PARAMETERS

Group 1			
Parameter	Value	Parameter	Value
U_{in}	200V	f_{CC}	107kHz
f_{QCV}	110.8kHz	L_1	142.5μH
L_2	125.7μH	M	33.52μH
L_{f1}	69μH	L_{f2}	29.6μH
C_{f1}	32.7nF	C_{f2}	76.1nF
C_1	30.8nF	C_2	23.5nF
Group 2			
Parameter	Value	Parameter	Value
U_{in}	200V	f_{CC}	99kHz
f_{CV}	115kHz	L_1	122.9μH
L_2	138.75μH	M	33.52μH
L_{f1}	46μH	L_{f2}	42μH
C_{f1}	56.2nF	C_{f2}	61.5nF
C_1	33.6nF	C_2	26.7nF
Group 3			
Parameter	Value	Parameter	Value
U_{in}	200V	f_{CC}	99kHz
f_{CV}	113kHz	L_1	122.9μH
L_2	138.75μH	M	33.52μH
L_{f1}	46μH	L_{f2}	42μH
C_{f1}	56.2nF	C_{f2}	61.5nF
C_1	33.6nF	C_2	26.7nF

the current input and output indicators based on the proposed parameter design method (that is, considering the influence of bilateral impedance angles at the same time, the conditions of ZPA and constant voltage can be appropriately relaxed). In Group 2, the impedance angle design was not considered, only the constant voltage output was concerned. As for Group 3, the zero-input impedance angle and constant voltage output were considered, but the magnitude of the secondary side impedance angle was not concerned. Groups 2 and 3 shared the same set of coils and compensation topology, but their operating frequencies (here, defined as f_{CV}) are different in CVM. Three groups of experimental parameters are presented in Table I.

The experimental system designed in this article is shown in Fig. 11. In this figure, I is the auxiliary power source, which supplies power to the DSP controller. II is the main power source. III is the coupler and its corresponding compensation circuit. The plane square structure was adopted, and the external dimension is 300 mm×300 mm×6 mm. IV is the full bridge inverter. V is the rectifier. VI is an oscilloscope. VII is the sliding rheostat as the load. VIII is a power analyzer. The input voltage of the system is 200 V. The sliding rheostat is used to simulate the increase of the battery internal resistance during charging. Here,

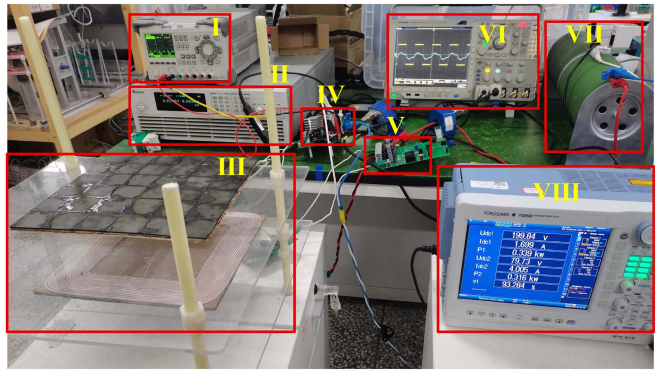

Fig. 11. Experimental prototype.

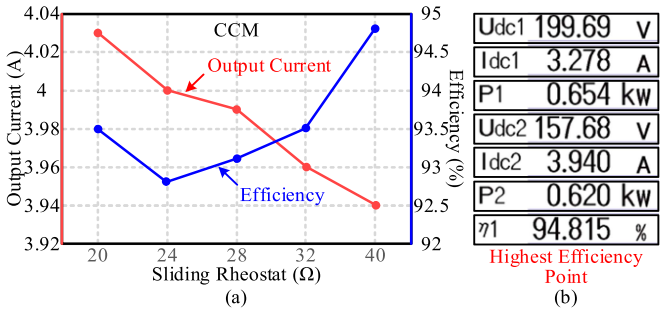

Fig. 12. Experimental data under CCM. (a) Output current and efficiency versus load. (b) Maximum efficiency point data of power analyzer.

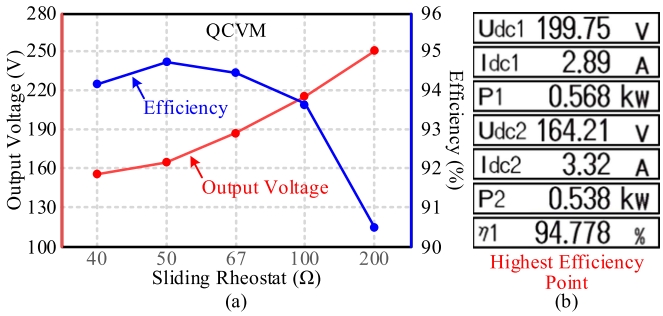

Fig. 13. Experimental data under QCVM. (a) Output voltage and efficiency versus load. (b) Maximum efficiency point data of power analyzer.

the simulated equivalent resistance increases from 20 to 40 Ω in CCM and from 40 to 200 Ω in QCVM.

Figs. 12(a) and 13(a) show the system output and corresponding efficiency of Group 1 in the case of CCM and QCVM, respectively. At the same time, in Figs. 12(b) and 13(b), the data on the power analyzer at the highest efficiency point in the corresponding mode are also given. When operating at 20 Ω with Group 1 parameters, the output voltage (U_{ab}) and output current (I_{Lf1}) of the inverter and the rectifier input voltage (U_{AB}) and input current (I_{Lf2}) are given in Fig. 14. Since the parameters of Groups 2 and 3 under CCM are the same, the corresponding working waveforms are almost the same. Therefore, only one is given here, as shown in Fig. 15, which also shows the working state at 20 Ω. It can be seen that the three groups of parameters all

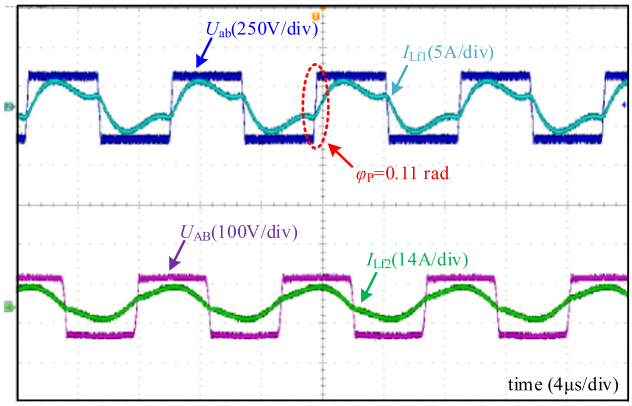

Fig. 14. Output current and voltage of the inverter and the input voltage and current of the rectifier of Group 1 when the load is 20 Ω.

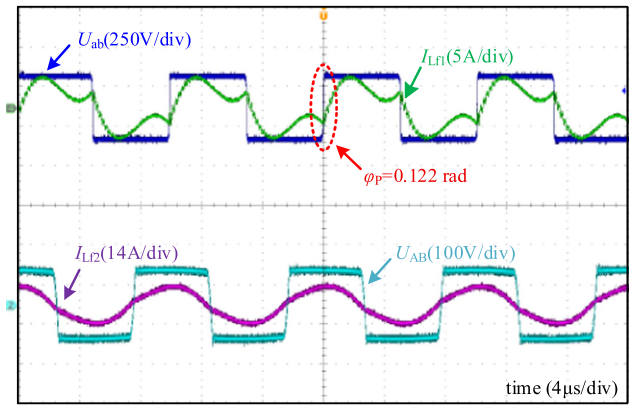

Fig. 15. Output current and voltage of the inverter and the input voltage and current of the rectifier of Groups 2 and 3 when the load is 20 Ω.

achieve a good resonance state under CCM, and the impedance angle of the primary side only retains a small value to facilitate the zero-voltage turn-ON of the inverter. In addition, more system performance comparisons are shown in Fig. 16. Among them, Fig. 16(a1)–(a4), (b1)–(b4), and (c1)–(c4) are the experimental results of Group 1, Group 2, and Group 3, respectively.

Fig. 16(a1), (b1), and (c1) shows the curves of the output current and output voltage versus load of Group 1, Group 2, and Group 3, respectively. It can be seen that the three groups of parameters have achieved good constant current output (4 A). In the whole process of CCM, the load is doubled, but the output current of Group 1 changes by only 2.23%. When the load is 40 Ω, the output current of Group 1 is 3.94 A, and the system efficiency reaches the highest value of 94.8% in this mode [see Fig. 12(b)]. Similarly, when the load is 40 Ω, the output current of Groups 2 and 3 is 4.08 A, and the system efficiency reaches the highest value of 94.3% [see Fig. 16(b2) and (c2)]. The output current of Groups 2 and 3 changes by only 1.21%. As for the constant voltage or quasi-constant voltage stage, when the load resistance changes from 40 to 200 Ω, the output voltage of Group 1 increases from 155 to 250 V, and the voltage fluctuation U_f is 0.47. The output voltage of Groups 2 and 3 is almost stable at 160 V, the voltage fluctuation is within 10V, and the U_f value is less than 0.05. All three groups of parameters meet the QCV conditions.

Fig. 16(a2), (b2), and (c2) shows the curves of the output power and system efficiency of Group 1, Group 2, and Group 3 versus load, respectively. When Group 1 works in CCM, as the load increases, the power increases from 322 to 621 W, the system efficiency also shows an upward trend. Since the system operates in resonant mode (that is, the primary and secondary impedance angles are both approximately 0), the efficiency fluctuation is relatively low, changing only 2%. When the load is 24 Ω, the system efficiency is the lowest at 92.8%. The similar conclusion can also be observed in the results of Groups 2 and 3 under CCM. When the load is 20 Ω, the system efficiency is the lowest at 90.2%. The output power and efficiency of the three groups of parameters are similar in CCM mode, and they all have achieved good results. However, when entering the CVM or the QCVM, the change in efficiency has a great difference. The efficiency of Group 1 always remains above 90%, with the highest value at 50 Ω (94.78%), and when the load changes to 200 Ω, the efficiency reaches the lowest point of 90.5%. As for Groups 2 and 3, although good constant voltage effect is achieved, they are much less efficient. Specifically, when Group 2 operates at the lowest output power, the efficiency has dropped to 60.1%, and when the load is 40 Ω, the efficiency is the highest but only 81.9%. There is a cliff-like drop in efficiency at the mode switching point, and the efficiency fluctuates wildly as the power drops. For Group 3, the power fluctuation is smaller than that of Group 2, with the highest efficiency (87.4%) at 50 Ω, but similarly, as the equivalent load resistance increases, the efficiency drops to a minimum of 77%. In addition, it can be found that in the vicinity of the maximum power point of the three groups of parameters (that is, within the equivalent load resistance variation range of 40–100 Ω), Group 1 is much better than the other two in terms of efficiency value and fluctuation degree, which is precisely benefited from the last consideration in the proposed design method (i.e., considering both the efficiency optimization around the maximum power point of the system and the maintenance of efficient robustness). Even far from the maximum power point (i.e., 200 Ω), the efficiency of Group 1 is still much higher than that of Groups 2 and 3. And this just verifies the rationality and effectiveness of the design method for efficiency optimization near the maximum power point. (As mentioned in the section on the proposed design method, when the efficiency at the maximum power point is improved, the efficiency at other power points will naturally be improved accordingly.)

As for the improvement of the maximum power point efficiency, it is closely related to the impedance angle of the primary and secondary sides at the corresponding moment. Fig. 16(a3), (b3), and (c3), respectively, shows the output voltage and output current of the inverter as well as the input voltage and current of rectifiers of Group 1, Group 2, and Group 3. Fig. 16(a4), (b4), and (c4) shows the currents of the primary and secondary coils of Group 1, Group 2, and Group 3, respectively. The test results are all the waveform corresponding to the maximum power load point at the constant voltage stage, namely 40 Ω. Because the secondary side input voltage is inconvenient to measure, an

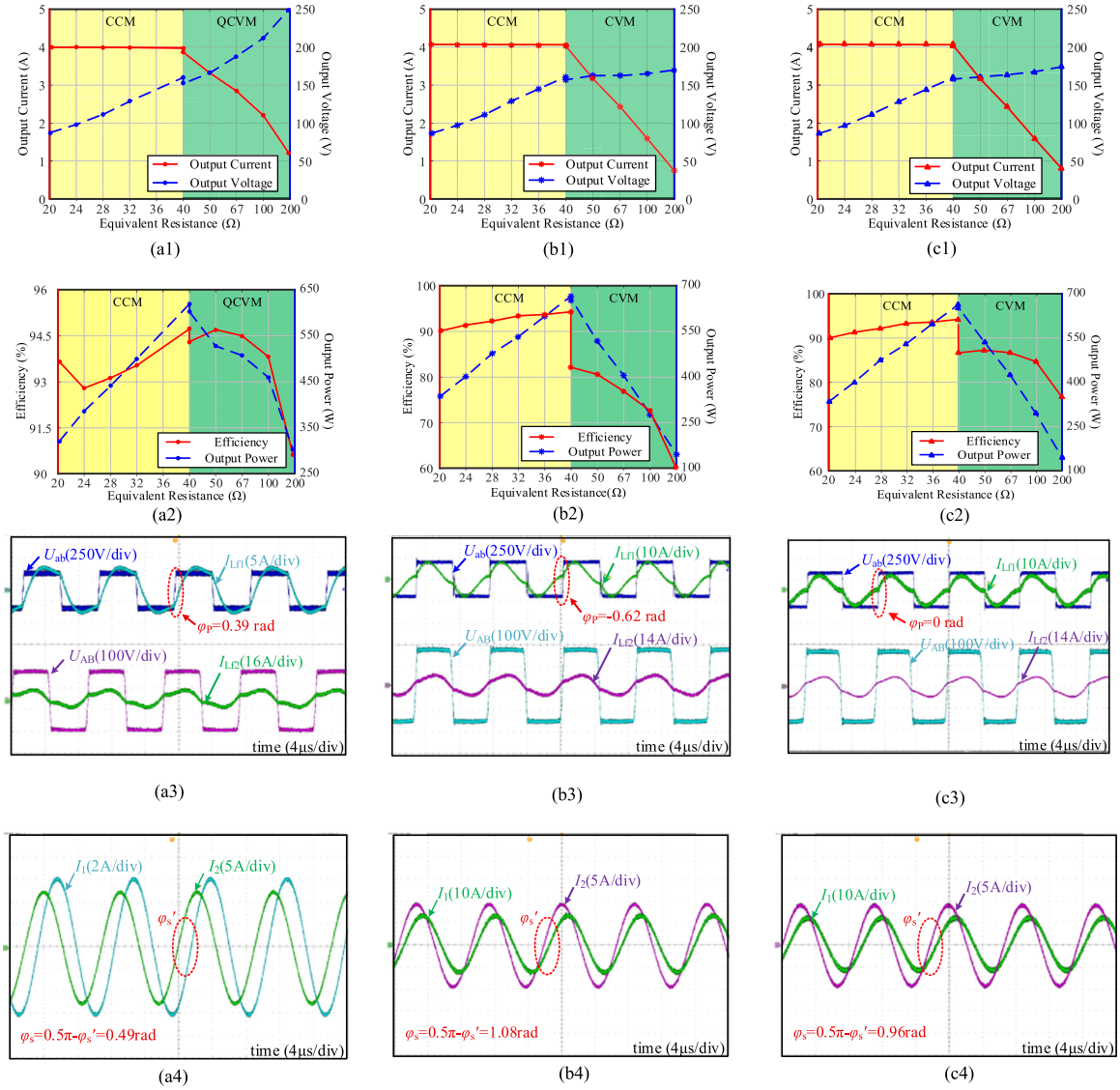

Fig. 16. Experimental results. (a) Group 1: (a1) output current and voltage versus load, (a2) output power and efficiency versus load, (a3) output current and voltage of the inverter and the input voltage and current of the rectifier when the load is 40 Ω under QCVM, (a4) primary and secondary coil current when the load is 40 Ω under QCVM. (b) Group 2: (b1) output current and voltage versus load, (b2) output power and efficiency versus load, (b3) output current and voltage of the inverter and the input voltage and current of the rectifier when the load is 40 Ω under CVM, (b4) primary and secondary coil current when the load is 40 Ω under CVM. (c) Group 3: (c1) output current and voltage versus load, (c2) output power and efficiency versus load, (c3) output current and voltage of the inverter and the input voltage and current of the rectifier when the load is 40 Ω under CVM, (c4) primary and secondary coil current when the load is 40 Ω under CVM.

indirect measurement method was adopted (i.e., by measuring the secondary side current). According to the voltage source equivalent model (see Fig. 4), the secondary input voltage U_2 can be expressed by

$$U_2 = \mathrm{j}\omega_{\mathrm{QCV(CV)}} M I_1, \omega_{\mathrm{QCV(CV)}} = 2\pi f_{\mathrm{QCV(CV)}}. \quad (27)$$

From this, it can be seen that the secondary side input voltage U_2 is ahead of the primary current I_1 by 90°. Here, define the angle at which the secondary current I_2 leads the primary current I_1 as φ_s'. Therefore, the secondary phase angle can be expressed as

$$\varphi_s = 0.5\pi - \varphi'_s. \quad (28)$$

The measured impedance angle values are also marked in the corresponding figures. It can be seen that the primary and secondary impedance angles of Group 1 are 0.39 and 0.49 rad, respectively, which is very close to the preset value (i.e., φ_p = 0.40 rad and φ_s = 0.485) in the proposed parameter design method mentioned above. The inverter not only achieves good zero-voltage turn-ON but also maintains a high level of system efficiency due to the low impedance angle of the primary and secondary sides. At the same time, as the equivalent load rises, the fluctuation in efficiency is also at a small level, as expected.

As for Group 2, although a good constant voltage effect has been achieved, due to the parameter design (namely, the reservation of weak inductance is not considered), it led to the situation where the primary impedance angle is less than zero (i.e., $\varphi_p = -0.62$ rad), which eventually resulted in a serious hard switching problem of the inverter. At this time, the current will lead the voltage, the energy of the parasitic capacitance

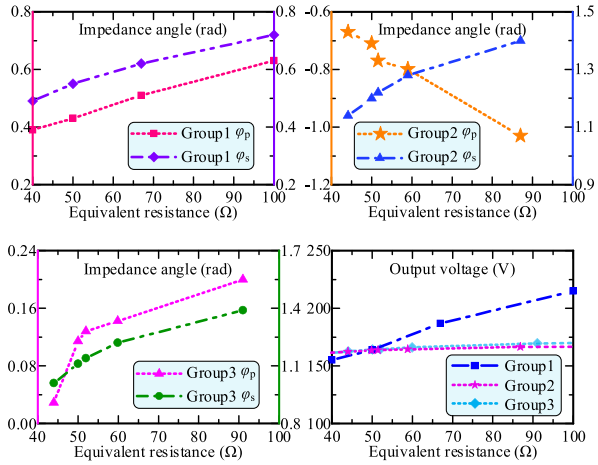

Fig. 17. Impedance angle and output voltage versus the equivalent load.

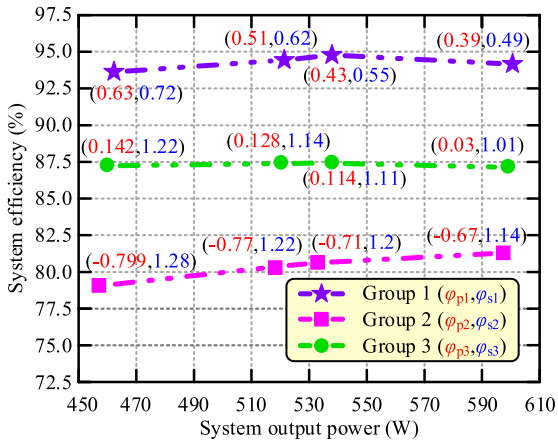

Fig. 18. Comparison of experimental results of three groups of parameters under the same power.

of the switch tube cannot be released, the dead time is almost useless, and the switching loss is extremely high. The oscillation phenomenon during voltage switching can be clearly seen from Fig. 16(b3). Furthermore, the secondary impedance angle that is not considered in advance reaches 1.08 rad, resulting in more reactive power loss to the system. Therefore, in Group 2, although all aspects of the system are in good condition under CCM, the problem of a cliff-like drop in efficiency occurred once CVM is entered. Correspondingly, the efficiency of other power points also deteriorated. Compared with the design of Group 2, the zero-impedance angle of the primary side was realized in Group 3 to maintain a better operating efficiency of the inverter. Therefore, when the mode is switched, the efficiency of Group 3 is higher than that of Group 2, and the oscillation phenomenon of hard switching did not appear in the inverter. But similarly, in the design of Group 3, although the ZPA and constant voltage output effects are guaranteed, the magnitude of the secondary impedance angle is still ignored. At the mode switching point, φ_s has reached 0.96 rad, which also brought a lot of reactive power loss. Through the efficiency comparison, the effect of Group 3 is actually worse than that of Group 1 (experimental parameters under the proposed design method). Correspondingly, at other power load points, the effect of Group 1 is also better than that of Group 3.

In order to further demonstrate the influence of the impedance angle on the system efficiency, Fig. 17 shows the magnitude of the impedance angle of the primary and secondary sides changing with the equivalent load under the three sets of parameters. Fig. 18 shows the system efficiency of different parameter groups and the corresponding impedance angle under the same output power. It can be clearly seen that the efficiency of Group 1 is much better than the other two. That is to say, considering the value of the double-sided impedance angle near the maximum power point and appropriately relaxing the ZPA and constant voltage output conditions is a reasonable and feasible efficiency optimization method.

The following is an analysis of capacitive stress and power loss distribution for Group 1 operating at maximum output power in QCVM. Fig. 19 shows the voltage stress on the primary and secondary compensation capacitors. The voltage peaks of the

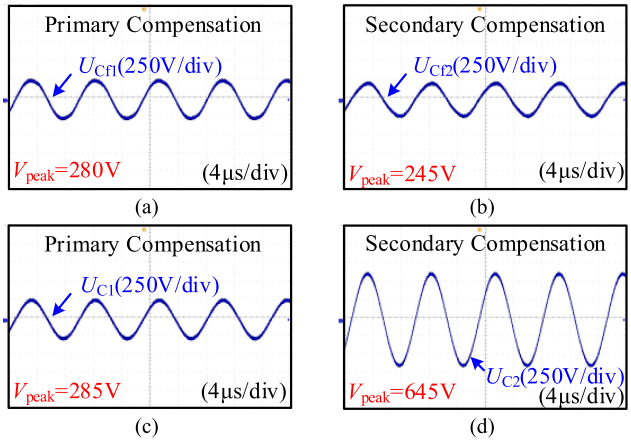

Fig. 19. Compensation capacitor voltage waveforms for Group 1 operating at maximum power point in QCVM. (a) Primary parallel capacitor C_{f1}. (b) Secondary parallel capacitor C_{f2}. (c) Primary series capacitor C_1. (d) Secondary series capacitor C_2.

TABLE II
COMPENSATION NETWORK PARASITIC RESISTANCE (GROUP 1)

Parameter	Parasitic resistance	Parameter	Parasitic resistance
L_1	150mΩ	C_{f1}	88mΩ
L_2	134mΩ	C_{f2}	46mΩ
L_{f1}	215mΩ	C_1	45mΩ
L_{f2}	111mΩ	C_2	60mΩ

series and parallel compensation capacitors on the primary side are 285 and 280 V, respectively, whereas those on the secondary side are 645 and 245 V. Furthermore, the parasitic resistance and power loss distribution of each part are shown in Table II and Fig. 20, respectively. It can be seen that although the total loss of the coil and compensation components is relatively high, up to 62.3%, this is inevitable for high-order compensation networks. The loss of the inverter is relatively low, which is mainly due to the fact that the system achieves better soft switching in Group 1. As for the efficiency of the rectifier, it can be further improved by synchronous rectification control.

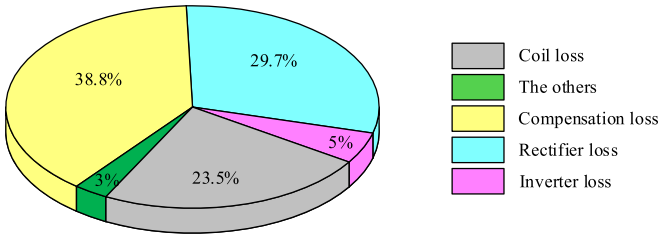

Fig. 20. System loss distribution diagram for Group 1 operating at maximum power point in QCVM.

VI. Conclusion

In this article, a novel method based on double side impedance angle design to optimize the efficiency of WPT systems is proposed. Compared with the scheme that only considers ZPA and constant voltage effect in the traditional design, in the proposed design method, the above conditions are appropriately relaxed under QCVM, and the influence of the primary and secondary impedance angles on the system efficiency is fully considered. Specifically, the overall efficiency is optimized by compressing the bilateral impedance angle around the maximum power point. In addition, the expression of the impedance angle is deduced in detail and the corresponding simplified formula is also given. The quasi-constant voltage convergence condition and the impedance angle limit range of the system are determined according to the voltage regulation capability, the target optimization efficiency, and the executable range of the parameters. At the same time, combined with the analysis of the sensitivity of the impedance angle relative to the system efficiency, it is finally determined that the parameter group that can achieve relatively high efficiency and keep the efficiency relatively stable is the optimal result, namely Group 1. In order to verify the effectiveness and feasibility of the proposed method, an experimental prototype based on the double-sided *LCC* topology and the planar square coils was built. Three comparative experiments were conducted. In CCM, the experimental results under the three sets of parameters all performed well. However, after switching the frequency to enter the CVM or QCVM, the system efficiency has a great difference due to the difference in the impedance angle. Although Group 1 is inferior to the other two groups in constant voltage output effect, it is superior in terms of system efficiency and robustness. In addition, the effectiveness of the proposed design method is further proved by the efficiency comparison of the three groups of parameters at the same power level.

References

[1] B. Zhang, X. Shu, and R. Huang, "The development of inductive and resonant wireless power transfer technology," *Trans. China Electrotech. Soc.*, vol. 32, no. 18, pp. 3–17, 2017.

[2] Y. Li and V. Jandhyala, "Design of retrodirective antenna arrays for short-range wireless power transmission," *IEEE Trans. Antennas Propag.*, vol. 60, no. 1, pp. 206–211, Jan. 2012.

[3] Y. Hu, X. Yuan, G. Zhang, and A. Schmeink, "Sustainable wireless sensor networks with UAV-enabled wireless power transfer," *IEEE Trans. Veh. Technol.*, vol. 70, no. 8, pp. 8050–8064, Aug. 2021.

[4] J. Liu et al., "Research and application of wireless sensor network technology in power transmission and distribution system," *Intell. Converged Netw.*, vol. 1, no. 2, pp. 199–220, 2020.

[5] B. Luo, T. Long, L. Guo, R. Dai, R. Mai, and Z. He, "Analysis and design of inductive and capacitive hybrid wireless power transfer system for railway application," *IEEE Trans. Ind. Appl.*, vol. 56, no. 3, pp. 3034–3042, May/Jun. 2020.

[6] Y. Huang, C. Liu, Y. Xiao, and S. Liu, "Separate power allocation and control method based on multiple power channels for wireless power transfer," *IEEE Trans. Power Electron.*, vol. 35, no. 9, pp. 9046–9056, Sep. 2020.

[7] J. Stillig, M. Edviken, and N. Parspour, "Overview and aspects of foreign object detection in wireless power transfer applications," in *Proc. IEEE Wireless Power Transf. Conf.*, 2020, pp. 380–383.

[8] A. J. Moradewicz and M. P. Kazmierkowski, "Contactless energy transfer system with FPGA-controlled resonant converter," *IEEE Trans. Ind. Electron.*, vol. 57, no. 9, pp. 3181–3190, Sep. 2010.

[9] J. Sallan, J. L. Villa, A. Llombart, and J. F. Sanz, "Optimal design of ICPT systems applied to electric vehicle battery charge," *IEEE Trans. Ind. Electron.*, vol. 56, no. 6, pp. 2140–2149, Jun. 2009.

[10] X. Qu, H. Han, S.-C. Wong, C. K. Tse, and W. Chen, "Hybrid IPT topologies with constant current or constant voltage output for battery charging applications," *IEEE Trans. Power Electron.*, vol. 30, no. 11, pp. 6329–6337, Nov. 2015.

[11] S. Wang et al., "Optimisation design for series–series dynamic WPT system maintaining stable transfer power," *IET Power Electron.*, vol. 10, no. 9, pp. 987–995, 2017.

[12] X. Qu, Y. Jing, H. Han, S.-C. Wong, and C. K. Tse, "Higher order compensation for inductive-power-transfer converters with constant-voltage or constant-current output combating transformer parameter constraints," *IEEE Trans. Power Electron.*, vol. 32, no. 1, pp. 394–405, Jan. 2017.

[13] R. Mai, Y. Chen, Y. Li, Y. Zhang, G. Cao, and Z. He, "Inductive power transfer for massive electric bicycles charging based on hybrid topology switching with a single inverter," *IEEE Trans. Power Electron.*, vol. 32, no. 8, pp. 5897–5906, Aug. 2017.

[14] C. Auvigne et al., "A dual-topology ICPT applied to an electric vehicle battery charger," in *Proc. IEEE Int. Conf. Electron. Mach.*, Mar. 2012, pp. 2287–2292.

[15] J. Mai et al., "Analysis, design and optimization of the IPT system with LC filter rectifier featuring high efficiency," *IEEE Trans. Ind. Electron.*, vol. 69, no. 12, pp. 12829–12841, Dec. 2022.

[16] J. Mai, X. Zeng, Y. Yao, Y. Wang, and D. Xu, "Impedance analysis and design of IPT system to improve system efficiency and reduce output voltage or current fluctuations," *IEEE Trans. Power Electron.*, vol. 36, no. 12, pp. 14029–14038, Dec. 2021.

[17] J. Mai, X. Zeng, Y. Yao, Y. Wang, and D. Xu, "Improved winding and compensation methods for the multilayer coil in IPT system," *IEEE Trans. Ind. Electron.*, vol. 69, no. 5, pp. 5375–5380, May 2022.

[18] C. Zheng et al., "High-efficiency contactless power transfer system for electric vehicle battery charging application," *IEEE J. Emerg. Sel. Topics Power Electron.*, vol. 3, no. 1, pp. 65–74, Mar. 2015.

[19] H. Feng, T. Cai, S. Duan, J. Zhao, X. Zhang, and C. Chen, "An LCC compensated resonant converter optimized for robust reaction to large coupling variation in dynamic wireless power transfer," *IEEE Trans. Ind. Electron.*, vol. 63, no. 10, pp. 6591–6601, Oct. 2016.

[20] Y. Wang, Y. Yao, X. Liu, D. Xu, and L. Cai, "An LC/S compensation topology and coil design technique for wireless power transfer," *IEEE Trans. Power Electron.*, vol. 33, no. 3, pp. 2007–2025, Mar. 2018.

[21] W. Li, H. Zhao, S. Li, J. Deng, T. Kan, and C. C. Mi, "Integrated LCC compensation topology for wireless charger in electric and plugin electric vehicles," *IEEE Trans. Ind. Electron.*, vol. 62, no. 7, pp. 4215–4225, Jul. 2015.

[22] S. Li, W. Li, J. Deng, T. D. Nguyen, and C. C. Mi, "A double-sided LCC compensation network and its tuning method for wireless power transfer," *IEEE Trans. Veh. Technol.*, vol. 64, no. 6, pp. 2261–2273, Jun. 2015.

[23] J. Hou, Q. Chen, S.-C. Wong, C. K. Tse, and X. Ruan, "Analysis and control of series/series-parallel compensated resonant converter for contactless power transfer," *IEEE J. Emerg. Sel. Topics Power Electron.*, vol. 3, no. 1, pp. 124–136, Mar. 2015.

[24] J. Hou, Q. Chen, X. Ren, X. Ruan, S.-C. Wong, and C. K. Tse, "Precise characteristics analysis of series/series-parallel compensated contactless resonant converter," *IEEE J. Emerg. Sel. Topics Power Electron.*, vol. 3, no. 1, pp. 101–110, Mar. 2015.

[25] K. Song et al., "An impedance decoupling-based tuning scheme for wireless power transfer system under dual-side capacitance drift," *IEEE Trans. Power Electron.*, vol. 36, no. 7, pp. 7526–7536, Jul. 2021.
[26] Y. Lim, H. Tang, S. Lim, and J. Park, "An adaptive impedance-matching network based on a novel capacitor matrix for wireless power transfer," *IEEE Trans. Power Electron.*, vol. 29, no. 8, pp. 4403–4413, Aug. 2014.
[27] T. C. Beh, M. Kato, T. Imura, S. Oh, and Y. Hori, "Automated impedance matching system for robust wireless power transfer via magnetic resonance coupling," *IEEE Trans. Ind. Electron.*, vol. 60, no. 9, pp. 3689–3698, Sep. 2013.
[28] R. W. Porto, V. J. Brusamarello, L. A. Pereira, and F. R. de Sousa, "Fine tuning of an inductive link through a voltage-controlled capacitance," *IEEE Trans. Power Electron.*, vol. 32, no. 5, pp. 4115–4124, May 2017.
[29] K. Colak, E. Asa, M. Bojarski, D. Czarkowski, and O. C. Onar, "A novel phase-shift control of semibridgeless active rectifier for wireless power transfer," *IEEE Trans. Power Electron.*, vol. 30, no. 11, pp. 6288–6297, Nov. 2015.
[30] H.-R. Cha et al., "Double-sided LCC compensation topology with semi-bridgeless rectifier for wireless power transfer system," in *Proc. IEEE 10th Int. Conf. Power Electron. ECCE Asia*, 2019, pp. 1–6, doi: 10.23919/ICPE2019-ECCEAsia42246.2019.8796908.
[31] J. Lu et al., "Constant current and constant voltage outputs for double-sided LCC resonant tank in inductively coupled power transfer system," *Proc. Chin. Soc. Elect. Eng.*, vol. 39, no. 9, pp. 2768–2778, 2019, doi: 10.13334/j.0258-8013.pcsee.171794.
[32] D. Wang, X. Qu, Y. Yao, and P. Yang, "Hybrid inductive-power-transfer battery chargers for electric vehicle onboard charging with configurable charging profile," *IEEE Trans. Intell. Transp. Syst.*, vol. 22, no. 1, pp. 592–599, Jan. 2021.
[33] K. Song, Z. Zhang, K. Qian, K. Wang, J. Zhang, and C. Zhu, "Loss analysis and calculation of magnetic coupler in wireless charging system," in *Proc. IEEE 4th Int. Elect. Energy Conf.*, 2021, pp. 1–5.
[34] Y. Chen, H. Zhang, C.-S. Shin, C.-H. Jo, S.-J. Park, and D.-H. Kim, "An efficiency optimization-based asymmetric tuning method of double-sided LCC compensated WPT system for electric vehicles," *IEEE Trans. Power Electron.*, vol. 35, no. 11, pp. 11475–11487, Nov. 2020.
[35] T. Kan, F. Lu, T.-D. Nguyen, P. P. Mercier, and C. C. Mi, "Integrated coil design for EV wireless charging systems using LCC compensation topology," *IEEE Trans. Power Electron.*, vol. 33, no. 11, pp. 9231–9241, Nov. 2018.
[36] V.-B. Vu, D.-H. Tran, and W. Choi, "Implementation of the constant current and constant voltage charge of inductive power transfer systems with the double-sided LCC compensation topology for electric vehicle battery charge applications," *IEEE Trans. Power Electron.*, vol. 33, no. 9, pp. 7398–7410, Sep. 2018.

Zhan Sun (Student Member, IEEE) was born in Heilongjiang Province, China, in 1997. He received the B.S. and M.S. degrees in electrical engineering, in 2019 and 2021, respectively, from the Harbin Institute of Technology, Harbin, China, where he is currently working toward the Ph.D. degree in electrical engineering.

His research interests include wireless power transfer, magnetic coupling structure design, and high-frequency and very high frequency converters.

Jinwu Sun was born in Tianjin, China, in 1998. He received the B.S. degree in electrical engineering, in 2021, from the Harbin Institute of Technology, Harbin, China, where he is currently working toward the M.S. degree in electrical engineering.

His research interests include intermediate frequency and high-frequency wireless power transfer and high-frequency and very high frequency converters.

Yijie Wang (Senior Member, IEEE) was born in Heilongjiang Province, China, in 1982. He received the B.S., M.S., and Ph.D. degrees in electrical engineering from the Harbin Institute of Technology, Harbin, China, in 2005, 2007, and 2012, respectively.

From 2012 to 2014, he was a Lecturer with the Department of Electrical and Electronics Engineering, Harbin Institute of Technology, where from 2014 to 2017, he was an Associate Professor. Since 2017, he has been a Professor with the Department of Electrical and Electronics Engineering, Harbin Institute of Technology. His research interests include dc–dc converters, soft-switching power converters, power factor correction circuits, digital control electronic ballasts, and LED lighting systems.

Dr. Wang is an Associate Editor for the IEEE TRANSACTIONS ON INDUSTRIAL ELECTRONICS, IEEE JOURNAL OF EMERGING AND SELECTED TOPICS IN POWER ELECTRONICS, IEEE ACCESS, *IET Power Electronics*, and *Journal of Power Electronics*.

Dianguo Xu (Fellow, IEEE) received the B.S. degree in control engineering from Harbin Engineering University, Harbin, China, in 1982, and the M.S. and Ph.D. degrees in electrical engineering from the Harbin Institute of Technology (HIT), Harbin, China, in 1984 and 1989, respectively.

In 1984, he joined the Department of Electrical Engineering, HIT, as an Assistant Professor. Since 1994, he has been a Professor with the Department of Electrical Engineering, HIT. From 2000 to 2010, he was the Dean of the School of Electrical Engineering and Automation, HIT. He was the Vice President of HIT from 2014 to 2020. He authored/coauthored more than 600 technical papers. His research interests include renewable energy generation technology, power quality mitigation, sensorless vector controlled motor drives, and high-performance servo system.

Dr. Xu is a Chairman of IEEE Harbin Section, Co-EIC of IEEE TRANSACTIONS ON POWER ELECTRONICS, and an Associate Editor for the IEEE TRANSACTIONS ON INDUSTRIAL ELECTRONICS and IEEE JOURNAL OF EMERGING AND SELECTED TOPICS IN POWER ELECTRONICS. He was the recipient of the 2018 IEEE IAS Outstanding Achievement Award.